

Article

Energy Storage and CO₂ Reduction Performances of Co/Co₂C/C Prepared by an Anaerobic Ethanol Oxidation Reaction Using Sacrificial SnO₂

Young In Choi ^{1,†}, Ju Hyun Yang ^{2,3,†}, So Jeong Park ² and Youngku Sohn ^{1,2,3,*} ¹ Department of Chemistry, Yeungnam University, Gyeongsan, Gyeongbuk 38541, Korea; cyi9161@naver.com² Department of Chemistry, Chungnam National University, Daejeon 34134, Korea; mil03076@naver.com (J.H.Y.); jsjs5921@naver.com (S.J.P.)³ Department of Chemical Engineering and Applied Chemistry, Chungnam National University, Daejeon 34134, Korea

* Correspondence: youngkusohn@cnu.ac.kr; Tel.: +82-42-821-6548

† These authors equally contributed to this work.

Received: 5 September 2020; Accepted: 22 September 2020; Published: 25 September 2020



Abstract: Co/Co₂C/C hybrids were prepared employing a new synthetic route and demonstrated as materials for energy storage and CO₂ recycling application. Herein, an anaerobic ethanol oxidation reaction over Co₃O₄ nanoparticles (NPs) was first employed to fabricate Co/Co₂C/C hybrids using sacrificial SnO₂. In the absence of SnO₂, Co₃O₄ NPs were converted to alpha and beta metallic Co. On the other hand, using sacrificial SnO₂ resulted in the formation of Co₂C and Co embedded in the carbon matrix at approximately 450 °C, as determined by temperature-programmed mass spectrometry analysis. The newly developed materials were fully examined by X-ray diffraction crystallography, scanning electron microscopy, energy-dispersive X-ray analysis, high-resolution transmission electron microscopy, and X-ray photoelectron spectroscopy. The Co/Co₂C/C hybrids showed a specific capacitance of 153 F/g at a current density of 0.5 A/g. Photocatalytic CO₂ reduction experiments were performed and generated CO, CH₄, and CH₃OH as reduction products with yields of 47.7, 11.0, and 23.4 μmol/g, respectively. The anaerobic ethanol oxidation reaction could be a very useful method for the development of carbon-supported metal carbides, which have not been achieved by other synthetic methods. Furthermore, the demonstration tests unveiled new application areas of Co carbide materials.

Keywords: Co/Co₂C/C hybrids; anaerobic ethanol oxidation; CO₂ reduction; specific capacitance; energy storage

1. Introduction

Cobalt carbide (Co₂C) and carbon-based materials have been usefully employed in diverse areas, such as chemical industry, energy industry, and environmental catalysts [1–6]. Co₂C has been extensively studied as a catalyst in photocatalytic hydrogen evolution [1], Fischer–Tropsch synthesis [7–12], hydrogen storage [13], water reduction electrocatalysis [14], and CO₂ conversion [15]. Guo et al. introduced metallic Co₂C as a cocatalyst for cadmium selenide (CdSe) quantum dots in hydrogen evolution reaction. They showed that when metallic Co₂C was coupled with CdSe quantum dots, the photocatalytic H₂ evolution activity increased to 18,000 μmol·g⁻¹·h⁻¹ (λ = 450 nm), which was 10 times more compared with that with bare CdSe [1]. Dong et al. prepared active carbon-supported Co–Co₂C catalysts for Fischer–Tropsch synthesis and showed a high catalytic activity for the hydroformylation of 1-hexene at low pressure [3]. Gao et al. showed that Co₃C nanoparticles (NPs), prepared by direct ball milling of Co and graphene, showed an electrochemical hydrogen storage

capacity of $1415 \text{ mA}\cdot\text{h}\cdot\text{g}^{-1}$ (5.176 wt% hydrogen) [13]. Kawashima et al. employed carbon-coated Co–Co carbide ($\text{Co-Co}_x\text{C}$, Co_xC : Co_2C , and Co_3C) composites for electrochemical hydrogen evolution reaction (HER) and achieved an overpotential of 78 mV at a current density of $10 \text{ mA}\cdot\text{cm}^{-2}$ and a Tafel slope of $87.8 \text{ mV}\cdot\text{dec}^{-1}$ [14]. Guo et al. used flowerlike Co_2C for the synthesis of cyclic carbonates by cycloaddition of CO_2 with epoxides and showed yields of up to 95% under solar light [15].

For the enhancement of Co_2C catalytic performance, various factors have been considered. For electrochemical application such as HER, crystalline phase and electrical conductivity are major factors for improving catalytic activity [1,14], where an active facet enhances efficient interfacial charge transfer [1]. For Co_2C nanoparticles in the Fischer–Tropsch synthesis of olefins, the activity and selectivity decreased as the particle size decreased from 7 nm [8]. Above 7 nm, the performances were nearly constant irrespective of the particle size. It is known that the sensitivity and selectivity are dependent on the exposed crystal facets [9,11], which are also determined by particle size in the nanosize region [8]. The catalytic activity was found to depend on the ratio of Co_2C to Co. $\text{Co}^0/\text{Co}_2\text{C}(111)$ is known to have dual active sites: Co^0 for CO dissociation and chain propagation and $\text{Co}_2\text{C}(111)$ for CO nondissociative activation and insertion [11]. The relative composition and exposed crystal facets of Co_2C were found to depend on the reaction pressure; consequently, the syngas conversion performance was greatly influenced by the pressure [11].

For the fabrication of Co and Co_2C , various synthesis methods include carburization [4], pulsed-spray evaporation (using alcohols) chemical vapor deposition (CVD) method process [16], pulsed plasma in liquid ethanol method [17], laser-induced irradiation method [18], polyol method and ball milling [13], spark plasma sintering [19], and laser ablation [20]. A previous report showed that the solvent (e.g., methanol, ethanol, and n-propanol) and the substrate temperature (with a working temperature below $300 \text{ }^\circ\text{C}$) determined the composition and crystallinity of Co and Co_2C . Co_2C can be prepared by the carburization of Co with CO for $>400 \text{ h}$ at $200 \text{ }^\circ\text{C}$ [4]. Pola et al. prepared Co, Co_2C , and Co_3C nanograins embedded in the carbon matrix, such as hexagonal graphite, by the infrared laser-induced irradiation of Co under gaseous hydrocarbon (e.g., benzene and ethylene) atmosphere [18]. Co carbide NPs, with a magnetic moment of 47 emu/g , were prepared by a modified polyol method at $\sim 300 \text{ }^\circ\text{C}$ using Co acetate tetrahydrate, NaOH, and polyvinylpyrrolidone in tetraethylene glycol [21]. Kamal et al. employed a spark plasma sintering method for the in situ decomposition of cobalt acetate, resulting in the formation of Co and Co_2C [19]. Metallic Co and Co_2C phases were formed at 30 and 60 MPa, respectively, and a mixed phase was formed at 45 MPa [19]. Zhang et al. showed that onionlike carbon-encapsulated Co_3C core/shells ($\sim 22 \text{ nm}$) could be prepared by the laser ablation of metallic Co in acetone [20]. Hasin showed that a mixture of graphene oxide and Co_3O_4 under $\text{H}_2\text{--N}_2$ gas stream at $200 \text{ }^\circ\text{C}$ was converted to Co_2C with a crystallite size of around 5 nm [22]. Motivated by the existing literature, it was demonstrated to find more efficient ways of preparing Co and Co_2C embedded in the carbon matrix; thus, an anaerobic ethanol oxidation reaction method was introduced. The advantage of using anaerobic ethanol oxidation reaction over other literature synthesis methods is that it is possible to make a bulk carbon fiber matrix where metal carbides are embedded. Therefore, a desirable high electrical conductivity can be achieved. In addition, Co/ Co_2C ratio could be controlled by varying the amount of sacrificial SnO_2 . It was found that the introduction of sacrificial SnO_2 was an important factor for the determination of the relative composition and formation of Co_2C . The newly developed method using ethanol as a carbon source could be further used to fabricate various metal carbide-based materials supported in the carbon matrix. Furthermore, in the present study, energy storage and CO_2 reduction tests were demonstrated to show their possible application in new areas.

2. Results and Discussion

Co/ Co_2C /C hybrids were prepared by the ethanol oxidation reaction of Co_3O_4 NPs mixed with sacrificial SnO_2 under an anaerobic condition. Figure 1 shows the XRD patterns of the prepared samples with different amounts of SnO_2 . The XRD patterns show a drastic difference due to the difference in SnO_2 content. In the absence of SnO_2 , peaks corresponding to two phases of metallic Co and carbon

were observed in the XRD pattern. The peak at $2\theta = 26.2^\circ$ could be assigned to the (002) plane of graphite carbon (JCPDS 98-005-3781) [2]. Thus, metallic Co adopts two different phases (■ and o). The three peaks (o, open circle) at $2\theta = 44.2^\circ$, 51.5° , and 75.9° were assigned to the (111), (002), and (022) planes of the cubic α -Co phase (Fm-3m, JCPDS 98-005-3805), respectively. The other three peaks (■, closed square) at $2\theta = 41.6^\circ$, 44.3° , and 47.4° were assigned to the (010), (002), and (011) planes of the hexagonal β -Co phase (P63/mmc, JCPDS 98-004-4900), respectively [3]. The corresponding standard XRD patterns for the α -Co and β -Co phases are also shown in Figure 1. The peaks corresponding to Co_3O_4 were not observed due to a lack of oxygen supply during the reaction. The oxygen of Co_3O_4 appeared to be consumed for ethanol oxidation without addition of oxygen supply under an anaerobic condition. Therefore, no Co_3O_4 (undetectable by XRD) was observed, which is further discussed below. The addition of 1 mol% SnO_2 suppresses the formation of the hexagonal β -Co phase compared with that of the cubic α -Co phase. Interestingly, a new crystal phase was found. The new peaks (·, closed circle) that appeared at $2\theta = 37.0^\circ$, 41.3° , 42.6° , 45.7° , and 56.6° were assigned to the (011), (002), (111), (021), and (112) planes of orthorhombic cobalt carbide (Pmnn, JCPDS 1-072-1369), respectively [1,3,4,19]. The rough XRD quantification ratios of $\text{Co}_2\text{C}/\text{Co}$ were 0, 0.8, 0.9, and 1 for the 0, 1, 5, and 10 mol% samples, respectively. $\text{Co}_2\text{C}/\text{Co}$ ratio was increased as the amount of SnO_2 was increased. It appears that Sn acts as a catalyst material for the formation of Co_2C . However, the Co_3C phase was not observed, as can be seen in the reference patterns [21]. For samples containing 10 mol% SnO_2 , the XRD peaks were mostly due to the Co_2C phase and carbon. A small peak corresponding to the hexagonal β -Co phase was observed, but that corresponding to the α -Co phase was not observed. Moreover, the crystal phases of Sn and Sn oxide were also not observed, plausibly due to their low content and/or amorphous state [23].

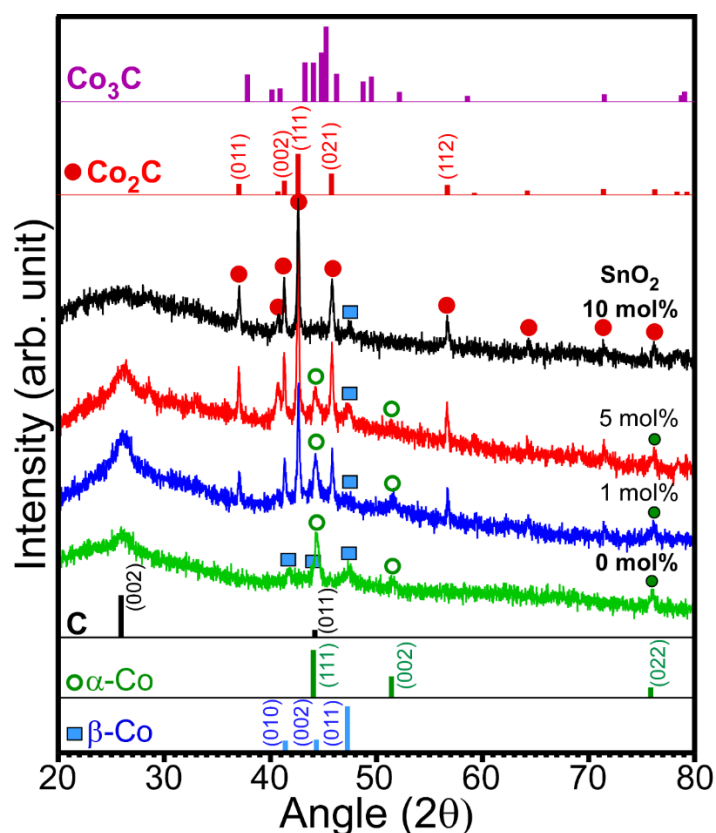


Figure 1. Powder X-ray diffraction patterns of the prepared samples with 0, 1, 5, and 10 mol% of sacrificial SnO_2 . Reference XRD patterns are displayed for β -Co (■), α -Co (o), C, Co_2C (●), and Co_3C .

The morphology and the microstructure were examined by electron microscopy. The scanning electron microscope (SEM) images showed at least three different morphologies of the samples, such as fibers and large and small particles (shown in Figure 2). The corresponding energy-dispersive X-ray (EDX) analysis spectra (not shown) showed the presence of the elements Co, C, and Sn [1]. The Co/C ratio decreased with the amount of Sn. The EDX atomic C%/Co% values were roughly estimated to be 98.7%/1.3%, 98.3%/1.7%, 94.8%/2.7%, and 92.5%/7.2% for the samples prepared with 0, 1, 5, and 10 mol% of sacrificial SnO₂, respectively. All the samples were mainly carbon species. The amounts of Sn, from the EDX data, were barely (below 0.3%) detected for the samples prepared with 5 and 10 mol% of sacrificial SnO₂. This indicates that the sacrificial SnO₂ played an important role in the formation of Co₂C. X-ray photoelectron spectroscopy (XPS) quantification for the 10 mol% sample was also performed and is shown later below. Briefly, Sn was estimated to be <0.2%, relative to the carbon. EDX elemental (C K and Co L) mapping images were obtained to discriminate the particles with various shapes and sizes from others. Sn elemental mapping signal was not detected because of extremely small amount. For the two mapping images of Co and C, the Co mapping image resembles more the SEM image. On the basis of the mapping images, the particles were concluded to be mainly Co species irrespective of the shapes. The Co species were appeared to be supported on the carbon species. The transmission electron microscope (TEM) and high-resolution transmission electron microscope (HR-TEM) images of the sample with 10 mol% of SnO₂ showed particle and fibrous morphologies of the sample. The Co species were covered by carbon fibers. In the TEM image, the fiber appeared like a tube [24]. For a particle, a clear lattice spacing of 0.213 nm corresponding to the (111) plane of orthorhombic Co₂C was observed [3,4,18]. The corresponding fast Fourier transform (FFT) pattern showed the (111) crystal plane. In HR-TEM, the round-shaped (or onionlike) area appeared to have been formed due to the stacking of bent graphite sheets [24]. A lattice spacing of 0.345 nm was a good match to the (002) plane of graphitic carbon [25].

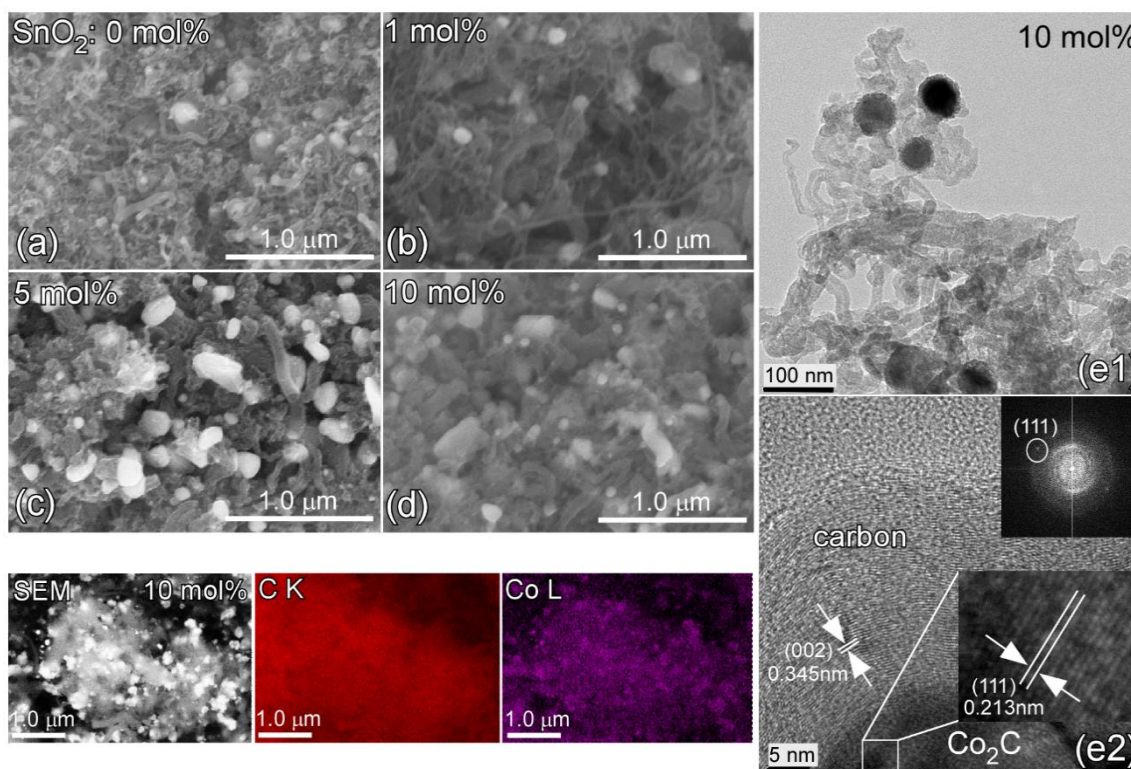


Figure 2. SEM (a–d), TEM (e1), and HR-TEM (e2) images of the prepared samples with 0, 1, 5, and 10 mol% of sacrificial SnO₂. Elemental (C K and Co L) mapping and the corresponding SEM images for the 10 mol% sample are shown.

Figure 3 shows the survey and normalized high-resolution XPS profiles of the sample with 10 mol% SnO₂ and depicts the surface chemical states of the newly fabricated sample. The survey spectrum for the as-prepared sample shows the elements C, Co, Sn, and O. Carbon was predominantly observed as expected (Figure 2). The atomic percentages for C, O, Co, and Sn were estimated to be 93.7%, 4.47%, 1.63%, and 0.2%, respectively. In the Sn 3d XPS profile, two peaks were observed at binding energies (BEs) of 495.3 eV (Sn 3d_{3/2}) and 486.8 eV (Sn 3d_{5/2}), with a spin-orbit splitting of 8.5 eV, plausibly due to Sn⁴⁺ of SnO₂ [23]. The weak shoulder observed at approximately 485.5 eV (Sn 3d_{5/2}) could be due to metallic Sn. The corresponding O 1s XPS peak was observed at 530.2 eV (inset Figure 3). A strong C 1s XPS peak at 284.6 eV was attributed to sp² elemental carbon (e.g., carbon nanotube). The other broad peak spanning from 286 to 292 eV was due to C-O, C=O, O=C-O, and $\pi \rightarrow \pi^*$ shake-ups, where - and = are single and double bonds, respectively [14,26]. In the Co 2p XPS profile, the Co 2p_{3/2} and Co 2p_{1/2} XPS peaks were observed at 781.3 and 796.9 eV, respectively, with a spin-orbit splitting of 15.6 eV, which can be attributed to Co²⁺ of Co₂C [1,14,26]. Moreover, two broad satellite peaks at approximately 788 and 804 eV confirmed the oxidation state of Co²⁺ [27]. Additionally, a narrow peak at 778.6 eV (Co 2p_{3/2}) confirmed the formation of metallic Co [1,14,18,27]. Based on the XPS data, it was confirmed that Co₂C and Co embedded in the carbon matrix were formed by the anaerobic ethanol oxidation reaction. XPS quantification was performed to examine the amounts of surface carbon, Co, and Sn species [28]. It was estimated that the amounts of Co and Sn were only 1.5% and <0.2% relative to that of carbon, respectively. This indicates that carbon was a main species and Co species were embedded in the carbon matrix. The rough EDX quantification above also showed that carbon was a main matrix species.

After CO₂ reduction of the corresponding samples, the high-resolution XPS profiles of C 1s, Co 2p, Sn 3d, and O 1s showed substantial changes (thick lines in Figure 3). The relative intensities of Co and O with respect to carbon were substantially increased after photocatalytic CO₂ reduction using a ultraviolet C (UVC) lamp. In the C 1s XPS profile, the major peak was observed at 284.3 eV. In addition, the broad region between 286 and 289 eV was somewhat increased, which can be attributed to increased signals of C-O, C=O, and O=C-O upon the adsorption of CO₂ and the species formed on reduction [14,26]. Interestingly, in the Co 2p XPS profile, the signal of metallic Co disappeared and the signal of Co 2p of Co²⁺ substantially increased. It appears that metallic Co changed to CoO after CO₂ reduction. In the Sn 3d XPS profile, the Sn 3d_{3/2} and Sn 3d_{5/2} peaks were substantially broadened and shifted to BEs of 496.1 and 487.6 eV, respectively, with a spin-orbit splitting of 8.5 eV. The broadness was plausibly due to the adsorption of CO₂ and Sn via O-Sn⁴⁺...O₂C, where ... is an interaction. In the O 1s XPS profile, two broad regions were observed, which may be attributed to the lattice oxygen of surface-oxidized Co at a lower BE of 530 eV and surface OH, C-O, and C=O at a higher BE of approximately 532.2 eV. The comparison of the normalized O 1s spectra before and after CO₂ reduction revealed that the intensity of the O 1s signal at a higher BE region was increased, similar to the C 1s spectra.

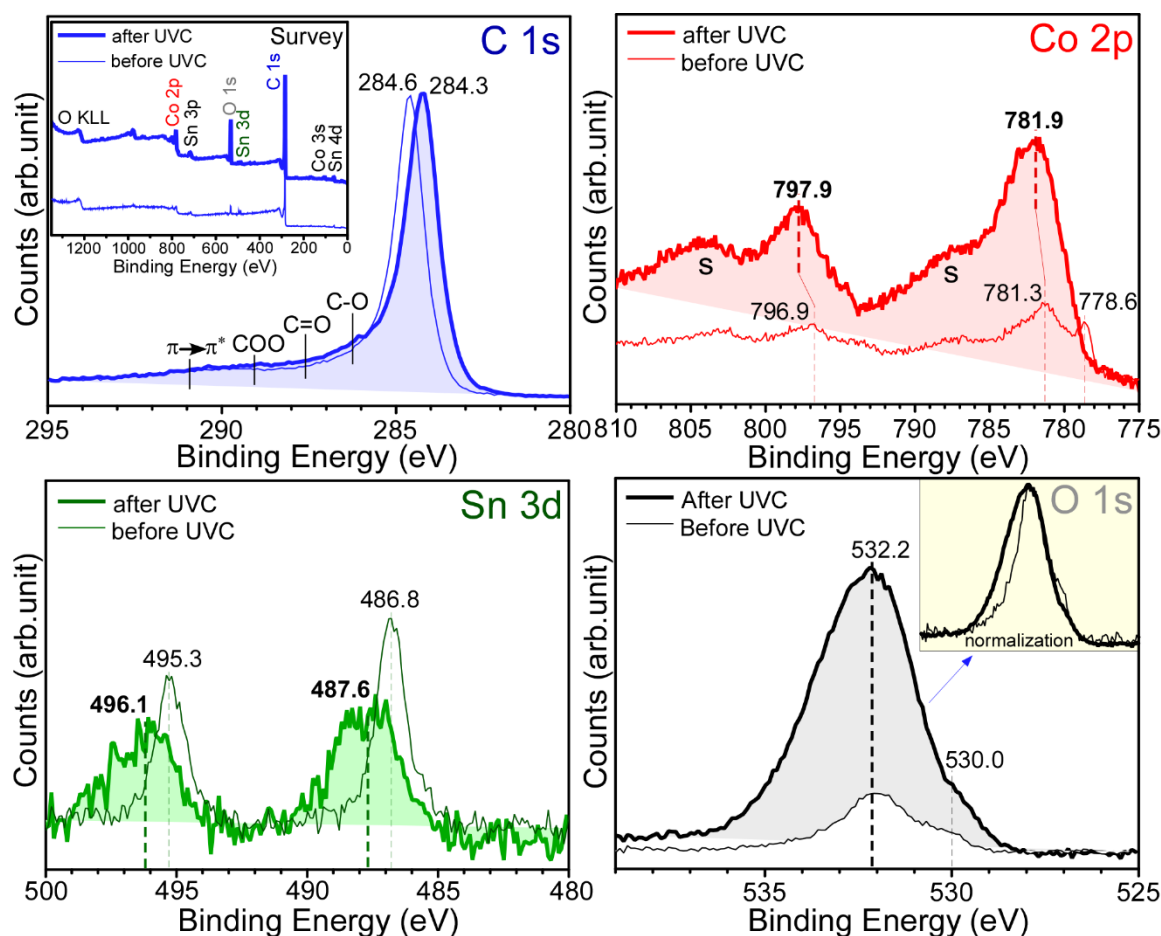


Figure 3. C 1s, Co 2p, Sn 3d, and O 1s XPS profiles of the selected (10 mol% SnO₂) sample before (thin line) and after (thick line) CO₂ reduction. The insets of C 1s and O 1s show survey XPS and normalized O 1s spectra, respectively.

Figure 4 displays typical mass profiles of the major gaseous products detected during the anaerobic ethanol oxidation reactions over the Co₃O₄ NPs mixed with 5 mol% SnO₂ NPs. The gaseous species include ethanol (46 amu), hydrogen (2 amu), methane (16 amu), water (18 amu), and carbon dioxide (44 amu). For the mass profiles with temperature, the temperature ramp rate was set to 20 °C/min within the range 25–600 °C. After the temperature reached 600 °C, the reaction was kept for 2 h. A slight increase in the mass signals of H₂, CH₄, and CO₂ began at approximately 200 °C, and the mass signals abruptly increased above 450 °C. At the same time, the mass signal of ethanol decreased, indicating that ethanol was significantly consumed in the catalytic reaction. The shapes of the mass profiles were all different. In the CO₂ and CH₄ mass profiles, there were two maxima below 600 °C, and two other maxima were found at 600 °C within 30 min. This indicates that the reaction channels were all different, and different solid catalyst species were formed at different temperatures. Kim et al. performed an anaerobic ethanol oxidation reaction over SnO₂ NPs and reported that H₂, H₂O, CO₂, and CH₄ were observed. In addition, their mass signals increased from 200 °C and showed a maximum at approximately 450 °C [23]. Based on the literature result, it was assumed that the gas products formed by adding sacrificial SnO₂ NPs could participate in catalyzing the CO₂C formation. On the basis of the mass profiles and the material analysis data, a general chemical equation can be written as CH₃CH₂OH + Co₃O₄ (and SnO₂) → a CO₂ (g) + b H₂O (g) + c CH₄ (g) + d H₂ (g) + Co₂C + Co (and Sn). Here, a simplified mechanism (where □ is Co₃O₄ or SnO₂) is proposed: ethanol is initially adsorbed and decomposes on the surface of metal oxides (e.g., Co₃O₄ and SnO₂ here) in reaction (1). The dissociatively adsorbed ethanol is further decomposed as the temperature is increased in reactions

(2), (3), and (4). Subsequently, H₂O, CO₂, CH₄, and H₂ are formed during the reactions. In reaction (5), metallic Sn or Co is formed by the reduction of the metal oxide due to adsorbed hydrogen. Adsorbed H can be associated to release molecular hydrogen in reaction (6). In the absence of an external oxygen supply, adsorbed CO (plausibly formed in reaction 2) can be participated in reducing metal oxides in reaction (7). Upon addition of SnO₂, metallic Sn was appeared to be more facile to be formed [23], compared with metallic Co. Therefore, it may catalyze the Co₂C formation. Co₂C could be formed via 2 Co + CH₄ → Co₂C + 2 H₂ in reaction (8) or 2 Co + CO + H₂ → Co₂C + H₂O in reaction (9) [29,30]. It has been reported that Co₃C could be formed in the range of 450–500 °C; however, the prepared Co₃C spontaneously decomposes to α-Co [2]. Co₂C is also known to decompose at above the temperature [29,30]. For this reason, Co₂C was appeared to be stably formed during the cooling stage when the temperature was below the equilibrium reaction temperature [2,29,30]. Co₃C could be formed via 3Co + CH₄ → Co₃C + 2H₂; however, the formation probability (relative to that of Co₂C) was low plausibly due to the non-stoichiometric ratio of Co/CH₄, which needs further investigation.

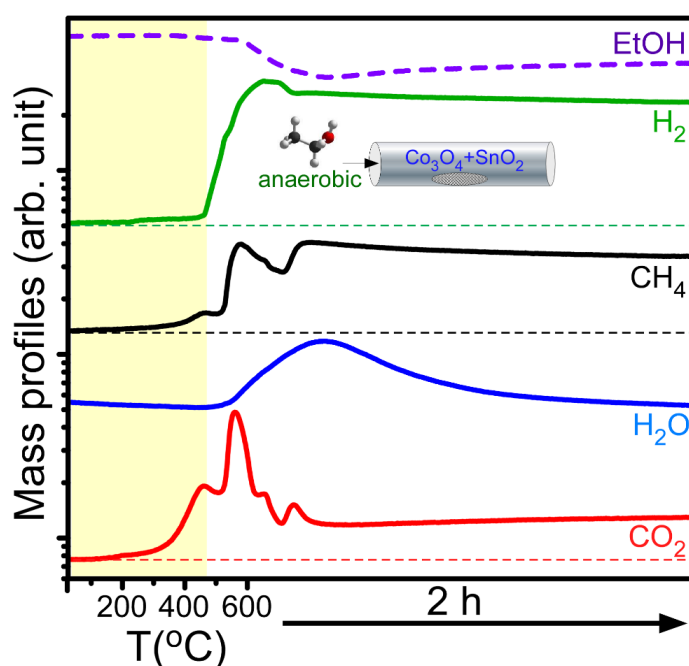
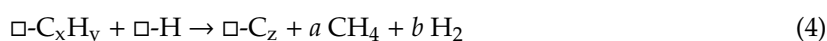
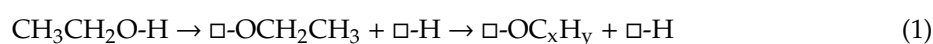


Figure 4. Mass profiles of the major gaseous products detected during the anaerobic ethanol oxidation reactions over the Co₃O₄ NPs mixed with 5 mol% SnO₂ NPs.

Pola et al. reported that Co, Co₂C, and Co₃C embedded in the carbon matrix were synthesized by IR laser-induced irradiation of Co in the presence of gaseous hydrocarbons [18]. Moreover, carbon film can be formed by the dehydrogenation and carbonization reactions of the hydrocarbons. Premkumar et al. employed a pulsed-spray evaporation CVD method to grow Co using cobalt acetylacetonate [16]. A mixture of Co carbide and metallic Co was formed below 250 °C when ethanol was used as a precursor solution. On the other hand, Co₂C was the dominant species when methanol or ethanol was used [16].

Figure 5 displays cyclic voltammetry (CV) curves, galvanostatic charge–discharge (CD) curves, and electrochemical impedance plots for the four different samples prepared with 0, 1, 5, and 10 mol% of sacrificial SnO₂. The CV curves were obtained between –0.2 and 0.7 V (vs. Ag/AgCl) in 6.0 M KOH at different scan rates of 10, 20, 40, and 80 mV/s. In general, the peak intensities in the CV curves increased with the increase in scan rate. For the sample without SnO₂, the oxidation and reduction peak width became substantially wider with increasing scan rate, indicating a diffusion-controlled electrode reaction [31]. Several peaks were observed due to the redox transformations Co ↔ Co(II), Co(II) ↔ Co(III), and Co(III) ↔ Co(IV) [31,32]. For the other three samples with additional Co₂C and SnO₂ species, additional cathodic and anodic peaks were observed. For the galvanostatic charge–discharge (CD) curves between 0.0 and 0.4 V (vs. Ag/AgCl), the CD time generally increased with increase in current density (Figure 5), as expected. The CD times were in the order 1.0 < 5.0 < 0.0 < 10.0 mol% SnO₂ at a fixed current density of 0.5 A/g. On the basis of the CD curves, the specific capacitance (C_m, F/g) was calculated using the expression $C_m = (I \cdot \Delta t) / (\Delta V \cdot m)$, where Δt is the discharge time (s), I is the discharge current (A), ΔV is the potential (V) range of 0.4 V, and m is the mass (g) of the sample [31,33]. At a current density of 0.5 A/g, the specific capacitances were calculated to be 101, 71, 93, and 153 F/g for the four different samples with 0, 1, 5, and 10 mol% SnO₂, respectively. Choi et al. previously reported a specific capacitance of ~100 F/g for Co₃O₄ nanostructures measured at a current density of 0.5 A/g [34]. The present value was comparable to the literature value measured under the same experimental conditions. This may indicate that Co/Co₂C/C hybrids can be a good supercapacitor material. The sample consisted of mainly Co₂C and carbon and showed the highest specific capacitance. To further extend the applicability of Co₂C supported in the carbon matrix, a long-term cycling stability test is needed. Electrochemical impedance spectroscopy (EIS) was employed, and the corresponding Nyquist plots (Figure 5) showed the real (Z') and imaginary (Z'') parts. Inset shows the plausible equivalent circuit model, where R_s, R_{ct}, Z_w, and double-layer capacitance (DLC) are bulk resistance, charge transfer resistance, Warburg resistance, and double-layer capacitance, respectively [35]. A semicircle in the high-frequency region and a straight line in the low-frequency region are generally attributed to the charge transfer resistant (R_{ct}) and the Warburg diffusion resistance (Z_w), respectively [31,34]. The intercept on the X-axis (real part, Z') is related with the bulk resistance (R_s) of electrolyte, separator, and electrodes. In the electrode/electrolyte system, R_{ct} and R_s were appeared to be dependent on the Co₂C/Co ratio in the carbon matrix. When the purity of Co or Co₂C was high, the resistance was observed to be low. The 0 and 10 mol% samples showed high purity with Co₂C/Co ratios of 0 and 1, respectively. The Co₂C/Co ratios for 1 and 5 mol% samples were estimated to be 0.8 and 0.9, respectively. Consequently, the lowest impure 1 mol% sample showed the highest resistance. The measured impedance data are in good consistency with the XRD Co₂C/Co quantification ratios as discussed above.

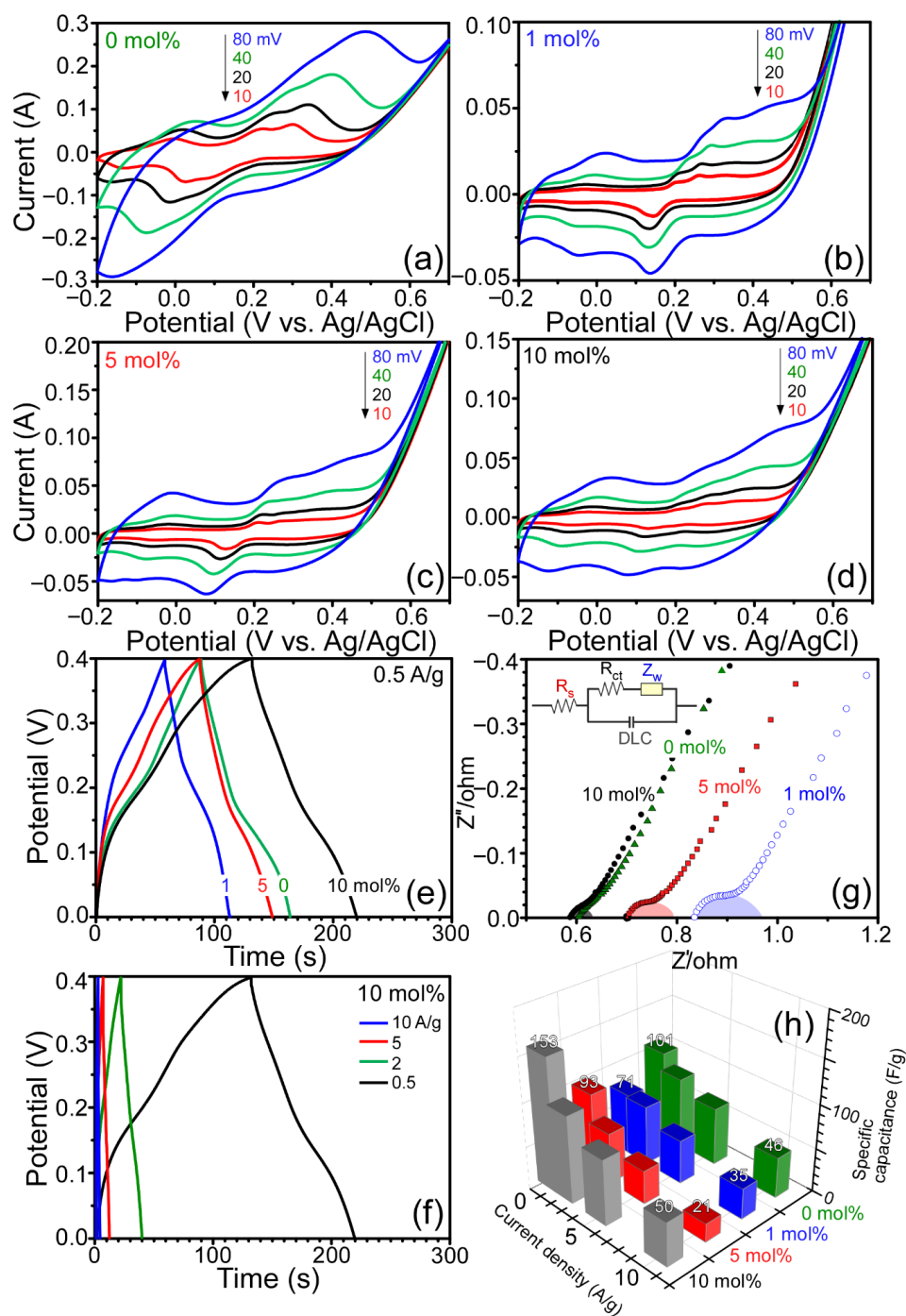
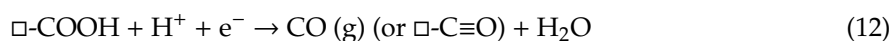


Figure 5. Cyclic voltammograms at various scan rates for (a) 0 mol%; (b) 1 mol%; (c) 5 mol%; (d) 10 mol% samples, (e) galvanostatic charge–discharge (CD) curves at 0.5 A/g for the four samples, (f) CD curves for the 10 mol% sample with different current densities, (g) Nyquist plots with the plausible equivalent circuit model, (h) the measured specific capacitances.

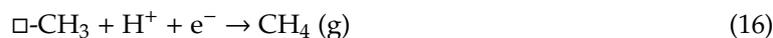
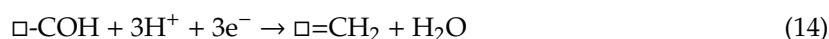
CO₂ reduction capability was also tested for bare Co₃O₄ and various Co/Co₂C/C hybrids under UVC irradiation for 13 h. CO, CH₄, and CH₃OH were commonly detected as CO₂ reduction products. For bare Co₃O₄, the yields of CO, CH₄, and CH₃OH were observed to be 83.2, 17.1, and 19.1 ppm (=μmol/mol), respectively. These values correspond to 48.9, 10.0, and 5.6 μmol/g, respectively. As the sacrificial SnO₂ content was increased, the amount of CO and CH₄ generated slightly decreased and then increased. The yields of CO, CH₄, and CH₃OH were observed to be 81.2, 18.7, and 79.8 ppm,

respectively, for Co_3O_4 with 10 mol% Sn. These values correspond to 47.7, 11.0, and 23.4 $\mu\text{mol/g}$, respectively. Interestingly, the production yield of CH_3OH constantly increased with the amount of sacrificial Sn. The yield increased by 4.2 times on the addition of 10 mol% Sn compared with that of bare Co_3O_4 . This indicates that Co/ Co_2C /C hybrids were beneficial for photocatalytic CH_3OH production. Additionally, smaller amounts of Sn may also contribute to the production. The hydrogen production channel is a major obstacle for increasing selectivity in CO_2 reduction. However, hydrogen evolution ($2\text{H}^+ + 2\text{e}^- \rightarrow \text{H}_2$) was not observed in the present study. CO_2 reduction commonly proceeds via multielectron transfer processes, where the electrons (e^-) are created by photoexcitation [36]. The holes (h^+) generated by photoexcitation undergo the reaction $2\text{H}_2\text{O} + 4\text{h}^+ \rightarrow \text{O}_2 + 4\text{H}^+$. Thereafter, CO_2 , e^- , and H^+ react to form CO, CH_3OH , and CH_4 via multielectron transfer reactions described below [36–38], where \square is a catalyst support.

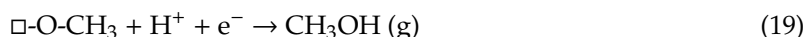
For CO generation via $\text{CO}_2 + 2\text{H}^+ + 2\text{e}^- \rightarrow \text{CO} + \text{H}_2\text{O}$:



For CH_4 generation via $\text{CO}_2 + 8\text{H}^+ + 8\text{e}^- \rightarrow \text{CH}_4 + 2\text{H}_2\text{O}$:



For CH_3OH generation via $\text{CO}_2 + 6\text{H}^+ + 6\text{e}^- \rightarrow \text{CH}_3\text{OH} + \text{H}_2\text{O}$:



The stability of Co/ Co_2C /C hybrids on CO_2 reduction was tested and is shown in Figure 6. The CO_2 reduction products became commonly decreased as the test cycle was increased. After the third test cycle, CO, CH_4 , and CH_3OH yields were decreased by 30%, 40%, and 70%, respectively. It may appear that the oxidation states (discussed in Figure 3) of Co/ Co_2C species were changed, and the surface states were deactivated on CO_2 reduction. Several Co-based photocatalysts on CO_2 reduction have been reported [39–41]; however, the literature on CO_2 reduction over Co_2C is not available. Jiang et al. introduced CuCo_2O_4 nanoplates as a photocatalytic CO reduction catalyst showing products of CO and H_2 , and a CO selectivity of 82% [39]. Gao et al. tested the photocatalytic CO_2 reduction efficiency for Co_3O_4 hexagonal platelets [40]. They reported CO and H_2 production rates of 2003 and 596 $\mu\text{mol}\cdot\text{h}^{-1}\cdot\text{g}^{-1}$, respectively, and a CO selectivity of 77.1%. Ren et al. reported a CO selectivity of 77.3% and a CO production rate of 39.70 $\mu\text{mol}\cdot\text{h}^{-1}$ for Co_3O_4 hierarchical nanosheets [41]. In all these cases, CH_4 and CH_3OH were not reported.

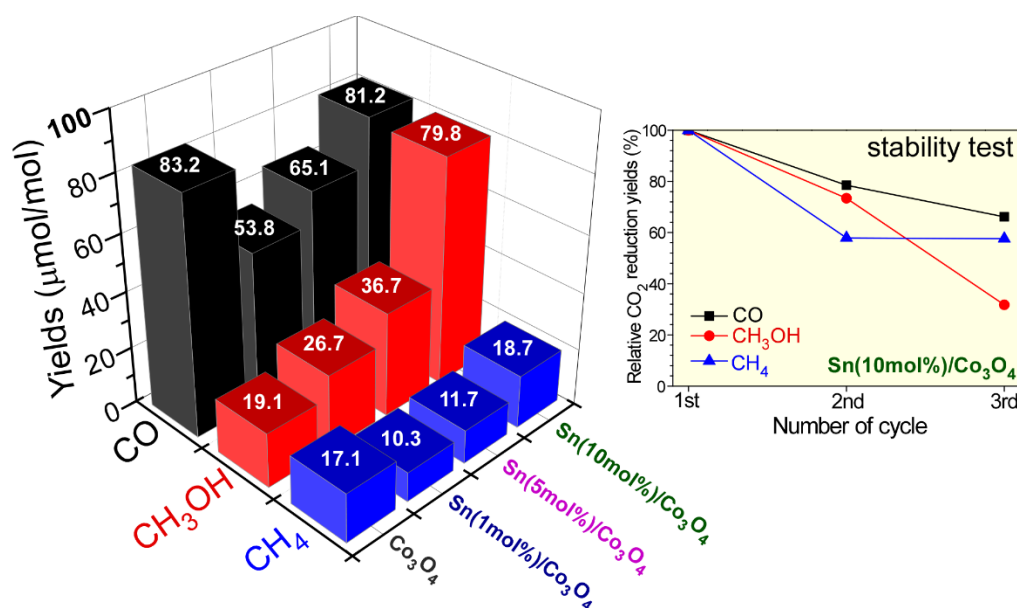


Figure 6. Photocatalytic total CO₂ reduction yields (μmol/mol) for the prepared samples with 0, 1, 5, and 10 mol% of sacrificial SnO₂, and the stability test (right panel) for the 10 mol% sample.

3. Materials and Methods

For the synthesis of Co₃O₄ NPs, 1.0 mmol of cobalt(II) nitrate hexahydrate (Acros Organics, 99.9%, Thermo Fisher Scientific, New Jersey, NJ, USA) was completely dissolved in 30 mL ethanol solvent followed by the addition of 2.0 mL of dimethylamine to the solution. The resulting solution was then tightly capped in a Teflon-lined stainless steel autoclave and kept at 180 °C for 12 h. Thereafter, the reaction vessel was cooled naturally to room temperature before collecting the resulting powder sample. The sample was repeatedly washed with deionized water and ethanol and dried at 80 °C. Thereafter, the dried sample was thermally treated at 350 °C for 3 h to obtain Co₃O₄ NPs. For the synthesis of Co/Co₂C/C nanostructures by the anaerobic ethanol oxidation reaction, 0.1 g of Co₃O₄ powder sample, mixed with 0, 1, 5, and 10 mol% SnO₂ powder, was first placed in a quartz U-tube (4 mm inner diameter, Quantachrome Instruments, Boynton Beach, FL, USA). Ethanol vapor was then introduced into the sample by flowing pure N₂ gas (99.99%) at the rate of 40 mL/min. During the introduction of ethanol vapor, the sample was heated to 600 °C at the rate of 20 °C/min. The sample was then kept at 600 °C for 2 h to complete the reaction. After the reaction, the reactor was naturally cooled to room temperature, and the introduction of ethanol vapor was stopped when the reactor temperature was below 150 °C. The gaseous products of the reaction were continuously monitored using an SRS RGA200 quadrupole mass spectrometer (Stanford Research Systems, Sunnyvale, CA, USA).

The morphology of the powder samples was examined using scanning electron microscopy (SEM; Hitachi S-4800, Tokyo, Japan) operating at an acceleration voltage of 10 keV. High-resolution transmission electron microscopy (HR-TEM) images of the powder samples on a carbon-coated Cu grid were recorded using a Tecnai G2 F20 S-TWIN microscope (FEL, Hillsboro, TX, USA) set at an acceleration voltage of 200 kV. Energy-dispersive X-ray (EDX) spectroscopy data were obtained using a Hitachi S-4200 SEM (Hitachi Ltd., Tokyo, Japan). The X-ray diffraction patterns (2θ angles from 20° to 80°) of the crystal phases of the newly synthesized powder samples were obtained using a PANalytical X'Pert Pro MPD diffractometer (Bruker Co., Ltd., Billerica, MA, USA) with Cu Kα radiation (40 kV and 30 mA). High-resolution XPS profiles were obtained using a Thermo Scientific K-Alpha spectrometer (Thermo VG Scientific, Waltham, MA, USA) with a monochromatic Al Kα X-ray source and a hemispherical energy analyzer.

Photocatalytic CO₂ reduction using a 15 W UVC lamp (a power density of 5.94 mW/cm²) was performed in a closed home-built stainless steel reactor, which was fully charged with CO₂ gas and

20 μL H_2O . A catalyst (3 mg) was dispersed on a quartz circular plate (a diameter of 45 mm) and placed in the reactor. After UVC light irradiation for 13 h, 0.5 mL of gas was taken and injected into a YL 6500 gas chromatograph (GC, Young In Chromass Co., Ltd., Seoul, Korea), which was equipped with a thermal conductivity detector (TCD), a flame ionization detector (FID), and a Ni catalyst methanizer.

For electrochemical and supercapacitor performance tests, a typical three-electrode system was employed, where a Pt wire (counter electrode), Ag/AgCl (3.0 M NaCl) reference electrode, and working electrode were connected electrically to a CHI660D (CH Instruments, Austin, TX, USA) electrochemical workstation. For the preparation of the working electrode, the synthesized powder material, acetylene black, and poly(vinylidene fluoride) (PVDF) at a weight ratio of 60:20:20, respectively, were completely dissolved in 2 mL of N-methyl-2-pyrrolidone (NMP) by grinding using an agate mortar. The sample ink was mounted onto a Ni foam (1×1 cm). The galvanostatic charge–discharge experiment was performed in a 6.0 M KOH aqueous solution over the potential range 0.0–0.4 V, with different charge densities (0.5, 1.0, 5.0, and 10.0 A/g). Electrochemical impedance spectroscopy (EIS) was conducted over the frequency range from 0.1 MHz to 0.01 Hz.

4. Conclusions

In the present study, an anaerobic ethanol oxidation reaction was first employed for the preparation of Co and Co_2C embedded in carbon matrices. In the absence of SnO_2 , Co_2C was not formed and only metallic (α and β) Co were formed in the carbon matrix. Interestingly, Co_2C was formed via the anaerobic ethanol oxidation reaction upon adding sacrificial SnO_2 . On the basis of the mass profiles of the gaseous products, a reaction mechanism was proposed for the formation of Co_2C . The addition of SnO_2 facilitated the production of H_2 and CH_4 . Subsequently, the produced CH_4 reacted with metallic Co to generate Co_2C . XRD, SEM, EDX analysis, HR-TEM, and XPS were employed to further characterize the newly prepared materials. The specific capacitance of Co/ Co_2C /C nanostructures reached 153 F/g at a current density of 0.5 A/g. The yields of CO, CH_4 , and CH_3OH , formed in photocatalytic CO_2 reduction, were observed to be 47.7, 11.0, and 23.4 $\mu\text{mol/g}$, respectively. This unique synthetic route for the formation of Co_2C in carbon support could be a very useful method for the development of carbon-supported Co carbide materials. In addition, the results for energy storage and CO_2 reduction experiments could open up new application areas.

Author Contributions: Y.S. designed the experiments and wrote the paper; Y.I.C., J.H.Y., and S.J.P., performed the experiments. All authors have read and agreed to the published version of the manuscript.

Funding: This work was financially supported by the National Research Foundation of Korea (NRF) grant funded by the Korean government (MEST) (NRF-2014R1A1A2055923 and NRF-2016R1D1A3B04930123). The APC was funded by NRF-2016R1D1A3B04930123.

Conflicts of Interest: The authors declare no conflict of interest.

References

1. Guo, Q.; Liang, F.; Gao, X.-Y.; Gan, Q.-C.; Li, X.-B.; Li, J.; Lin, Z.-S.; Tung, C.-H.; Wu, L.-Z. Metallic Co_2C : A promising co-catalyst to boost photocatalytic hydrogen evolution of colloidal quantum dots. *ACS Catal.* **2018**, *8*, 5890–5895. [[CrossRef](#)]
2. Aluha, J.; Abatzoglou, N. Activation and deactivation scenarios in a plasma-synthesized Co/C catalyst for Fischer-Tropsch synthesis. *Can. J. Chem. Eng.* **2018**, *96*, 2127–2137. [[CrossRef](#)]
3. Dong, W.; Liu, J.; Zhu, H.; Ding, Y.; Pei, Y.; Liu, J.; Du, H.; Jiang, M.; Liu, T.; Su, H.; et al. Co- Co_2C and Co- Co_2C /AC catalysts for hydroformylation of 1-hexene under low pressure: Experimental and theoretical studies. *J. Phys. Chem. C* **2014**, *118*, 19114–19122. [[CrossRef](#)]
4. Pei, Y.; Ding, Y.; Zang, J.; Song, X.; Dong, W.; Zhu, H.; Wang, T.; Chen, W. Temperature-programmed desorption and surface reaction studies of CO on Co_2C . *Chin. J. Catal.* **2013**, *34*, 1570–1575. [[CrossRef](#)]
5. Singh, J.A.; Hoffman, A.S.; Schumann, J.; Boubnov, A.; Asundi, A.S.; Nathan, S.S.; Nørskov, J.; Bare, S.R.; Bent, S.F. Role of Co_2C in ZnO-promoted Co catalysts for alcohol synthesis from syngas. *Chem. Cat. Chem.* **2019**, *11*, 799–800.

6. Xiong, S.; Chen, J.; Lou, X.; Zeng, H. Mesoporous Co_3O_4 and $\text{CoO}@C$ topotactically transformed from chrysanthemum-like $\text{Co}(\text{CO}_3)_{0.5}(\text{OH})\cdot 0.11\text{H}_2\text{O}$ and their lithium-storage properties. *Adv. Funct. Mater.* **2012**, *22*, 861–871. [[CrossRef](#)]
7. Wang, X.; Lin, T.; Li, J.; Yu, F.; Lv, D.; Qi, X.; Wang, H.; Zhong, L.; Sun, Y. Direct production of olefins via syngas conversion over Co_2C -based catalyst in slurry bed reactor. *RSC Adv.* **2019**, *9*, 4131–4139. [[CrossRef](#)]
8. Dai, Y.; Zhao, Y.; Lin, T.; Li, S.; Yu, F.; An, Y.; Wang, X.; Xiao, K.; Sun, F.; Jiang, Z.; et al. Particle size effects of cobalt carbide for Fischer–Tropsch to olefins. *ACS Catal.* **2019**, *9*, 798–809. [[CrossRef](#)]
9. Wang, B.; Liang, D.; Zhang, R.; Ling, L. Crystal facet dependence for the selectivity of C_2 species over Co_2C catalysts in the Fischer–Tropsch synthesis. *J. Phys. Chem. C* **2018**, *122*, 29249–29258. [[CrossRef](#)]
10. Zhao, Z.; Lu, W.; Yang, R.; Zhu, H.; Dong, W.; Sun, F.; Jiang, Z.; Lyu, Y.; Liu, T.; Du, H.; et al. Insight into the formation of $\text{Co}@C$ catalysts for direct synthesis of higher alcohols and olefins from syngas. *ACS Catal.* **2018**, *8*, 228–241. [[CrossRef](#)]
11. An, Y.; Lin, T.; Yu, F.; Wang, X.; Lu, Y.; Zhong, L.; Wang, H.; Sun, Y. Effect of reaction pressures on structure–performance of Co_2C -based catalyst for syngas conversion. *Ind. Eng. Chem. Res.* **2018**, *57*, 15647–15653. [[CrossRef](#)]
12. Zhang, R.; Wen, G.; Adidharma, H.; Russell, A.G.; Wang, B.; Radosz, M.; Fan, M. C_2 Oxygenate synthesis via Fischer–Tropsch synthesis on Co_2C and $\text{Co}/\text{Co}_2\text{C}$ interface catalysts: How to control the catalyst crystal facet for optimal selectivity. *ACS Catal.* **2017**, *7*, 8285–8295. [[CrossRef](#)]
13. Gao, P.; Wang, Y.; Yang, S.; Chen, Y.; Xue, Z.; Wang, L.; Li, G.; Sun, Y. Mechanical alloying preparation of fullerene-like Co_3C nanoparticles with high hydrogen storage ability. *Int. J. Hydrogen Energy* **2012**, *37*, 17126–17130. [[CrossRef](#)]
14. Kawashima, K.; Shin, K.; Wygant, B.R.; Kim, J.-H.; Cao, C.L.; Lin, J.; Son, Y.J.; Liu, Y.; Henkelman, G.; Mullins, C.B. Cobalt metal–cobalt carbide composite microspheres for water reduction electrocatalysis. *ACS Appl. Energy Mater.* **2020**, *3*, 3909–3918. [[CrossRef](#)]
15. Guo, Q.; Xia, S.-G.; Li, X.-B.; Wang, Y.; Liang, F.; Lin, Z.-S.; Tung, C.-H.; Wu, L.-Z. Flower-like cobalt carbide for efficient carbon dioxide conversion. *Chem. Commun.* **2020**, *56*, 7849–7852. [[CrossRef](#)] [[PubMed](#)]
16. Premkumar, P.A.; Turchanin, A.; Bahlawane, N. Effect of solvent on the growth of Co and Co_2C using pulsed-spray evaporation chemical vapor deposition. *Chem. Mater.* **2007**, *19*, 6206–6211. [[CrossRef](#)]
17. Chen, L.; Mashimo, T.; Iwamoto, C.; Okudera, H.; Omurzak, E.; Ganapathy, H.S.; Ihara, H.; Zhang, J.; Abdullaeva, Z.; Takebe, S.; et al. Synthesis of novel $\text{CoC}_x@C$ nanoparticles. *Nanotechnology* **2013**, *24*, 045602. [[CrossRef](#)]
18. Pola, J.; Urbanova, M.; Pokorna, D.; Subrt, J.; Bakardjieva, S.; Bezdicka, P.; Bastl, Z. IR laser-induced formation of amorphous $\text{Co}-C$ films with crystalline Co , Co_2C and Co_3C nanograins in a graphitic shell. *J. Photochem. Photobiol. A Chem.* **2010**, *210*, 153–161. [[CrossRef](#)]
19. Kamal, S.S.K.; Kumar, A.P.; Vimala, J.; RamaRao, N.V.; Majumdar, B.; Ghosal, P.; Durai, L. In situ synthesis of cobalt and cobalt carbide nanostructures using decomposition of cobalt acetate. *J. Alloy. Compd.* **2018**, *748*, 814–817. [[CrossRef](#)]
20. Zhang, H.; Liang, C.; Liu, J.; Tian, Z.; Shao, G. The formation of onion-like carbon-encapsulated cobalt-carbide core/shell nanoparticles by laser ablation of metallic cobalt in acetone. *Carbon* **2013**, *55*, 108–115. [[CrossRef](#)]
21. Zamanpour, M.; Bennet, S.P.; Majidi, L.; Chen, Y.; Harris, V.G. Process optimization and properties of magneticall hard cobalt carbide nanoparticles via modified polyol method. *J. Alloy. Compd.* **2015**, *625*, 138–143. [[CrossRef](#)]
22. Hasin, P. Low-temperature synthesis of mesoporous cobalt(II) carbide using graphene oxide as a carbon source. *J. Phys. Chem. C* **2014**, *118*, 4726–4732. [[CrossRef](#)]
23. Kim, W.J.; Lee, S.W.; Sohn, Y. Metallic Sn spheres and $\text{SnO}_2@C$ core-shells by anaerobic and aerobic catalytic ethanol and CO oxidation reactions over SnO_2 nanoparticles. *Sci. Rep.* **2015**, *5*, 13448. [[CrossRef](#)] [[PubMed](#)]
24. Luo, C.; Qi, X.; Pan, C.; Yang, W. Diamond synthesis from carbon nanofibers at low temperature and low pressure. *Sci. Rep.* **2015**, *5*, 13879. [[CrossRef](#)] [[PubMed](#)]
25. Chen, W.; Yu, Y.; Zheng, X.; Qin, S.; Wang, F.; Fang, J.; Wang, G.; Wang, C.; Wang, L.; Peng, G.; et al. All-carbon based graphene field effect transistor with graphitic electrodes fabricated by e-beam direct writing on PMMA. *Sci. Rep.* **2015**, *5*, 12198. [[CrossRef](#)]
26. Okpalugo, T.I.T.; Papakonstantinou, P.; Murphy, H.; McLaughlin, J.; Brown, N.M.D. High resolution XPS characterization of chemical functionalized MWCNTs and SWCNTs. *Carbon* **2005**, *43*, 153–161. [[CrossRef](#)]

27. Gwag, J.; Sohn, Y. Interfacial natures and controlling morphology of Co oxide nanocrystal structures by adding spectator Ni ions. *Bull. Korean Chem. Soc.* **2012**, *33*, 505–510. [[CrossRef](#)]
28. Seah, M.P.; Gilmore, I.S.; Spencer, S.J. Quantitative XPS. *J. Electron. Spectrosc. Relat. Phenom.* **2001**, *120*, 93–111. [[CrossRef](#)]
29. Huba, Z.J.; Carpenter, E.E. A versatile synthetic approach for the synthesis of CoO, Co_xC, and Co based nanocomposites: Tuning kinetics and crystal phase with different polyhydric alcohols. *CrystEngComm* **2014**, *16*, 8000–8007. [[CrossRef](#)]
30. Zhang, S.; Liu, X.; Shao, Z.; Wang, H.; Sun, Y. Direct CO₂ hydrogenation to ethanol over supported Co₂C catalysts: Studies on support effects and mechanism. *J. Catal.* **2020**, *382*, 86–96. [[CrossRef](#)]
31. Lee, S.; Kang, J.-S.; Leung, K.T.; Lee, W.; Kim, D.; Han, S.; Yoo, W.; Yoon, H.J.; Nam, K.; Sohn, Y. Unique multi-phase Co/Fe/CoFe₂O₄ by water-gas shift reaction, CO oxidation and enhanced supercapacitor performances. *J. Ind. Eng. Chem.* **2016**, *43*, 69–77. [[CrossRef](#)]
32. Garcia, E.M.; Taroco, H.A.; Matencio, T.; Domingues, R.Z.; dos Santos, J.A.F.; Ferreira, R.V.; Lorençon, E.; Lima, D.Q.; de Freitas, M.B.J.G. Electrochemical recycling of cobalt from spent cathodes of lithium-ion batteries: Its application as supercapacitor. *J. Appl. Electrochem.* **2012**, *42*, 361–366. [[CrossRef](#)]
33. Liu, X.; Liu, J.; Sun, X. NiCo₂O₄@NiO hybrid arrays with improved electrochemical performance for pseudocapacitors. *J. Mater. Chem. A* **2015**, *3*, 13900–13905. [[CrossRef](#)]
34. Choi, Y.I.; Yoon, H.J.; Kim, S.K.; Sohn, Y. Crystal-facet dependent CO oxidation, preferential oxidation of CO in H₂-rich, water-gas shift reactions, and supercapacitor application over Co₃O₄ nanostructures. *Appl. Catal. A* **2016**, *519*, 56–67. [[CrossRef](#)]
35. Choi, W.; Shin, H.-C.; Kim, J.M.; Choi, J.-Y.; Yoon, W.-S. Modeling and applications of electrochemical impedance spectroscopy (EIS) for lithium-ion batteries. *J. Electrochem. Sci. Technol.* **2020**, *11*, 1–13. [[CrossRef](#)]
36. Sohn, Y.; Huang, W.; Taghipour, F. Recent progress and perspectives in photocatalytic CO₂ reduction of Ti-oxide based nanomaterials. *Appl. Surf. Sci.* **2017**, *396*, 1696–1711. [[CrossRef](#)]
37. Sun, Z.; Ma, T.; Tao, H.; Fan, Q. Fundamentals and challenges of electrochemical CO₂ reduction using two-dimensional materials. *Chem* **2017**, *3*, 560–587. [[CrossRef](#)]
38. Shin, J.; Do, J.Y.; Kim, R.; Son, N.; Park, N.-K.; Ryu, H.-J.; Seo, M.W.; Chi, J.; Youn, Y.-S.; Kang, M. Catalytic activity of Ni_{1-x}Li_{2x}WO₄ particles for carbon dioxide photoreduction. *Catalysts* **2019**, *9*, 467. [[CrossRef](#)]
39. Jiang, M.; Gao, Y.; Wang, Z.; Ding, Z. Photocatalytic CO₂ reduction promoted by a CuCo₂O₄ cocatalyst with homogeneous and heterogeneous light harvesters. *Appl. Catal. B* **2016**, *198*, 180–188. [[CrossRef](#)]
40. Gao, C.; Meng, Q.; Zhao, K.; Yin, H.; Wang, D.; Guo, J.; Zhao, S.; Chang, L.; He, M.; Li, Q.; et al. Co₃O₄ Hexagonal Platelets with Controllable Facets Enabling Highly Efficient Visible-Light Photocatalytic Reduction of CO₂. *Adv. Mater.* **2016**, *28*, 6485–6490. [[CrossRef](#)]
41. Ren, J.-T.; Zheng, Y.-L.; Yuan, K.; Zhou, L.; Wu, K.; Zhang, Y.-W. Self-templated synthesis of Co₃O₄ hierarchical nanosheets from a metal–organic framework for efficient visible-light photocatalytic CO₂ reduction. *Nanoscale* **2020**, *12*, 755–762. [[CrossRef](#)] [[PubMed](#)]

